Supplementary Information

Frequency microcomb stabilization via dual-microwave control

Abhinav Kumar Vinod[1,*,+], Shu-Wei Huang[1,*,+], Jinghui Yang[1], Mingbin Yu[2], Dim-Lee Kwong[2], and Chee Wei Wong[1,*]

[1] Mesoscopic Optics and Quantum Electronics Laboratory, University of California Los Angeles, CA, USA

[2] Institute of Microelectronics, Singapore, Singapore

[*] abhinavkumar@ucla.edu; swhuang@seas.ucla.edu; cheewei.wong@ucla.edu

[+] these authors contributed equally to this work

Supplementary Note I: Other comb states

The comb state is generated with a New Focus Velocity TLB-6730 as the pump laser. The pump frequency is tuned with a 2 MHz step via fine piezo control. The general multiple mode-spaced (MMS) scheme of comb formation involves the generation of several subcomb families with incommensurate spacing between them [SR1, SR2]. This is illustrated in Supplementary Fig. S1a, as we might expect, combs evolving via this scheme would, in general, produce several low frequency RF beats. The comb state we stabilize however, is one with a single offset beat and has just one other subcomb family aside from the sub-comb around the primary comb line as illustrated in Supplementary Fig. S1b. This state is not a necessary part of the comb evolution process and is only observed under the right conditions of power and detuning. Here we briefly describe several other states that we observe in our microresonator. One of the comb states we have observed, generates an equally spaced set of beats spanning around 600 MHz. This 'RF comb' is shown in Supplementary Fig. S2a, in this particular case an interesting point to note is that although multiple subcomb families exist in this state, the RF beats being equally spaced indicates a relationship between the different subcomb families.

As detuning is changed this state changes to one with higher noise that does not show a regular equally spaced comb structure in the RF domain, as shown in Supplementary Fig. S2b. This state then eventually evolves into one with continuous low frequency noise, the RF spectrum at the repetition rate of such a comb is shown in Supplementary Fig. S2c. In addition, we observe states

similar to the one we use for stabilization, having a strong low frequency RF beat in addition to the beat due to f_{rep}, as shown in Supplementary Fig. S2d, but exhibiting slightly different behavior with regards to degree of correlation between pump and the offset beat.

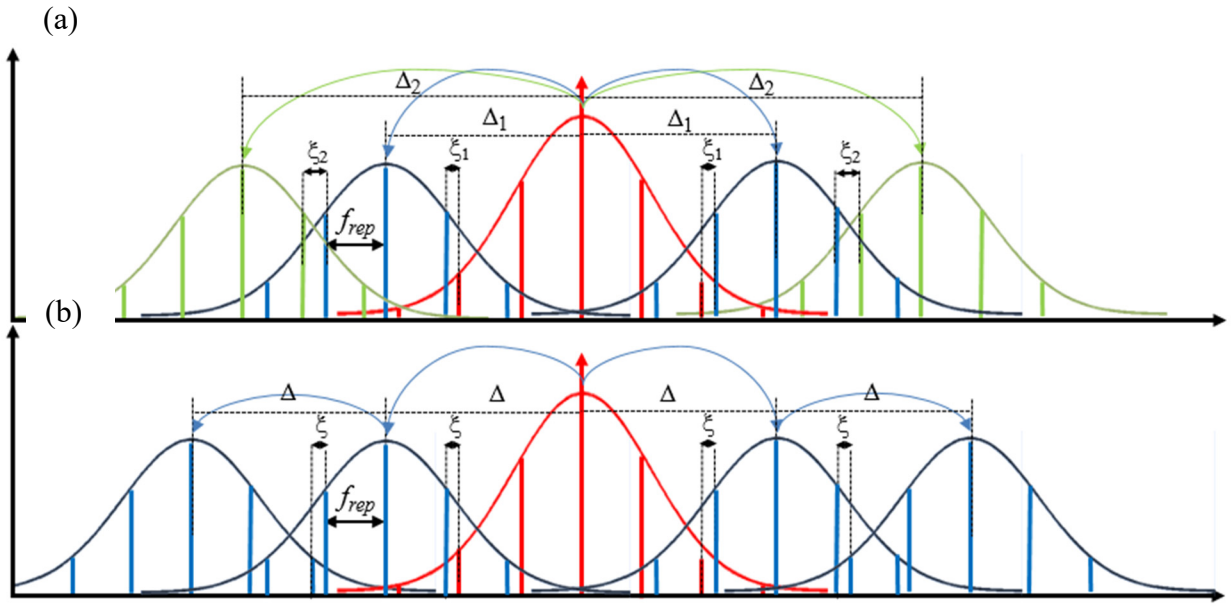

Supplementary Figure S1. a, The general MMS scheme of comb formation, the two sets of subcombs, shown in blue and green belong to different families because the two sets of primary comb lines around which the subcombs form, are generated independently by the pump. The first set of primary comb lines are formed at an offset of Δ_1 from the pump and the second set are formed at an offset of Δ_2 from the pump, since Δ_2 is not a multiple of Δ_1 and neither Δ_2 nor Δ_1 need be integral multiples of the f_{rep}, there are two offset beats generated by beating of subcombs with each other, these offset beats are shown in the schematic as ξ_1 and ξ_2. Now if this idea is extended to multiple subcomb families we would expect the generation of multiple RF beatnotes, (and if the subcombs were broad enough we would also generate harmonics of the beatnotes) and this is what we experimentally observe. **b,** A special case of MMS comb formation that results in the generation of a single RF beat note (aside from the beat due to f_{rep}) that corresponds to the offset ξ between subcombs. Note that, in this case, only the first set of primary comb lines is formed due to modulation instability via the pump, all other primary comb lines are generated via cascaded four-wave mixing between the pump and the first set of primary comb lines, this mechanism allows for a single offset ξ, throughout the comb. We choose to stabilize this particular state due to the strong correlation between the pump frequency and ξ due to the dependence of ξ on Δ, as described in the main text.

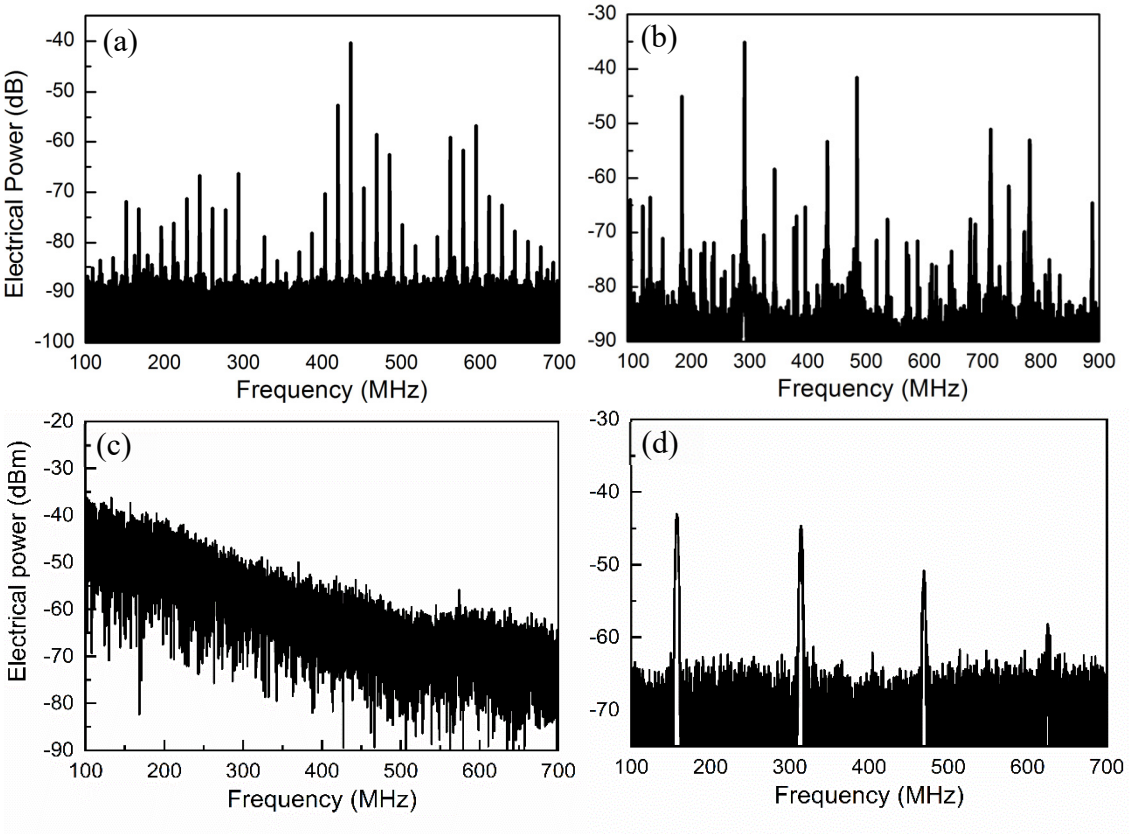

Supplementary Figure S2. a, Multiple RF beats spanning 600 MHz with a spacing of 16 MHz generated by a comb state. The beats being equally spaced indicates that there is correlation between the offsets of different subcomb families. **b,** Multiple RF beats spanning over a GHz, generated by a comb state. Lack of defined structure to the beats suggests a general MMS scheme for the evolution of the state **c,** RF spectrum showing continuous low frequency noise, this state is obtained from the state in b. by changing the detuning such that the number of RF beats keeps increasing till we eventually have a 'noise pedestal' of continuous noise. **d,** RF spectrum showing a strong offset beat (breather tone) along with multiple harmonics. This state is similar to the one we stabilize; except for the fact that it is less stable to change in pump power or detuning (there is a sudden transition to another state). It also exhibits different behavior with regards to degree of correlation between pump frequency and offset beat.

Supplementary Note II: Microresonator dispersion and comb spectrum

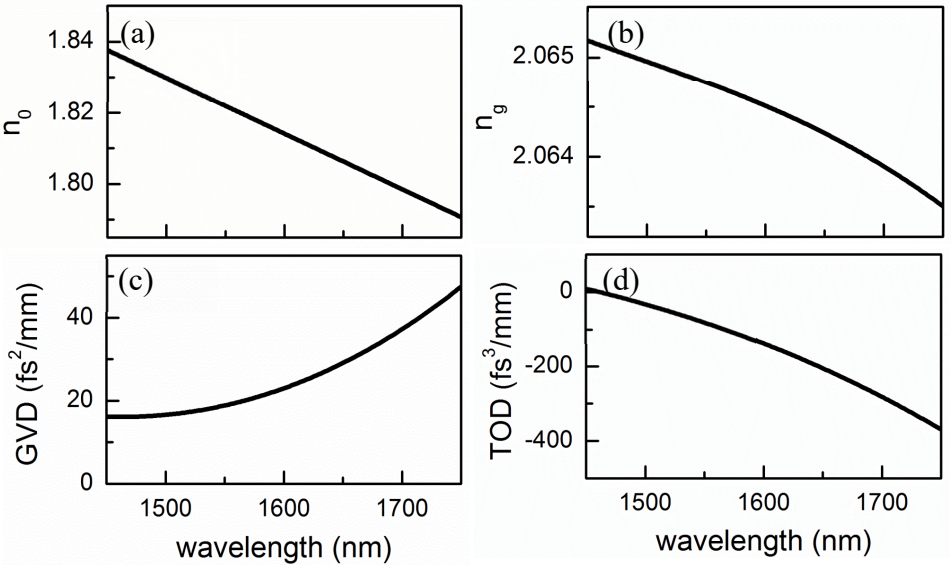

Supplementary Figure S3. Waveguide dispersion is calculated taking into account of both the material dispersion and the geometric dispersion. **a,** Refractive index n_o, measured at 1.81 at pump wavelength of 1598 nm. **b,** Group index n_g, measured at 2.064 at the pump wavelength. **c,** Group velocity dispersion (GVD) measured at 23 fs^2/mm at the pump wavelength. **d,** Third-order dispersion (TOD) measured at 265 fs^3/mm at pump wavelength of 1598 nm.

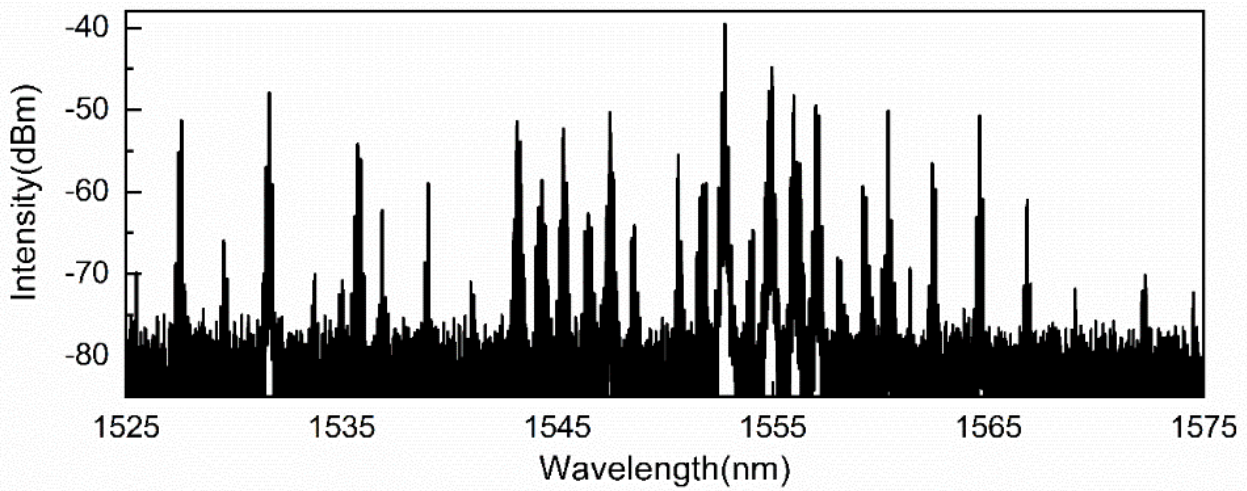

Supplementary Figure S4. Example filtered C-band frequency microcomb spectrum. Formation of primary comb lines with Δ = 1.1 nm and overlap between secondary comb lines are observed (left inset). Its electrical spectrum measures two distinct beat notes of f_{rep} = 17.9 GHz and ξ = 523.35 MHz (right inset). The highly modulated spectrum is due to mode disruptions every 4 nm, which periodically perturbs the GVD.

Supplementary Note III: Details of the measurement setup

The measurement setup is shown in Fig. 2 in the main text. The comb spacing is measured by sending a section of the comb to a high speed photodetector to directly detect the beat note from

the repetition rate f_{rep}. We then obtain the error signal for feedback by downmixing the output signal with a 17.9 GHz local oscillator. This error signal is the input to a PI^{2}D lock box with a bandwidth of 10 MHz, which sends the feedback signal to an EOM to modulate the input power of the 3W EDFA which pumps the microresonator. The EDFA is operated in the current control mode to achieve effective modulation of the output power, to within 1% and less than 0.1 dB. Even with the free-space alignment optics, the lock can be maintained for more than an hour in each measurement set. In a fully packaged system, the lock can likely be maintained for a longer time. We also note that, with higher microcavity Q, the microcomb threshold power can be lowered and microcombs, with the similar FSR as our demonstration, with tens of milliwatt pump power has been implemented entirely on chip [SR3, SR4].

In addition to power modulation via the EOM, we also have a secondary feedback signal (derived by integrating the primary feedback control signal) to the EDFA which directly modulates the power, relatively slowly, primarily with the objective to increase the dynamic range of the lock (EDFA is not used as the sole feedback because it cannot be operated at the full feedback bandwidth). The feedback is designed in the above manner, with fast feedback via the EOM for high feedback bandwidth and slow feedback via the EDFA for high dynamic range, to preserve an optimal lock for a long period of time. Supplementary Fig. S5 summarizes the quality of the f_{rep} stabilization. After the stabilization of the comb spacing, we notice that the offset beat ξ also becomes more stable as can be visually observed from Supplementary Fig. S6. This is per our expectation of partial correlation between ξ and f_{rep} as described in the main text.

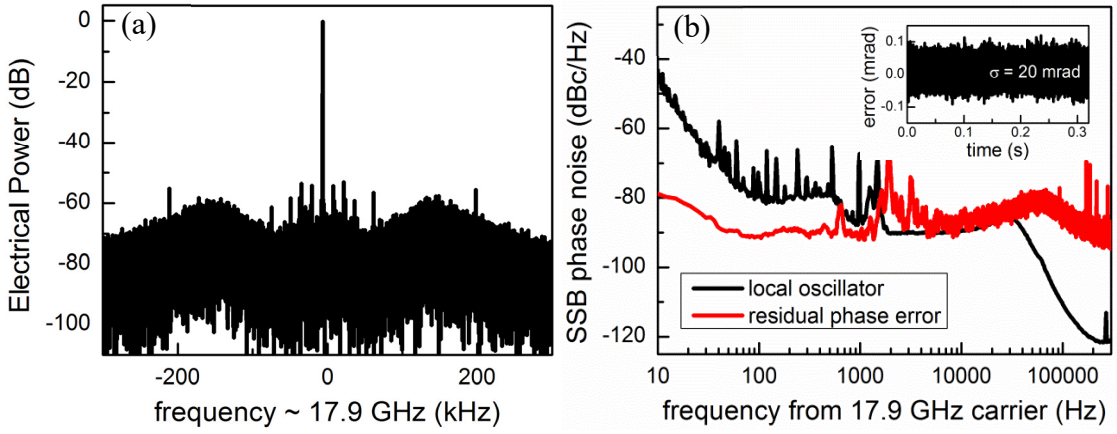

Supplementary Figure S5. a, RF spectrum of the stabilized beat note of f_{rep} with an RBW of 10 Hz. In the PI^{2}D loop filter, the PI corner and differential frequency were both set at 200 kHz. The design provides a delicate compromise between noise suppression and loop stability. A remaining small noise oscillation at 205 kHz, however, is still present. **b,** Single-sideband phase noise of the reference 17.9 GHz local oscillator and the residual error from the f_{rep} phase-locked loop, showing

an excess phase noise of the stabilized comb spacing above 40 kHz from carrier. Inset: rms phase error integrated from 6 Hz to 600 kHz is 20 mrad.

The offset frequency ξ can be used as an indicator of pump frequency after stabilization of f_{rep}, as explained in detail in the main text. We therefore use this signal to stabilize the pump frequency when the comb spacing is locked. To achieve a high SNR (which is required to lock ξ effectively), we use an optical grating filter to select a 1-nm section of the comb where the beat frequency is strongest and then send that section to a photodetector to detect the beat (SNR is higher because of a strong beat note in the localized region and also because the detector is not saturated by the f_{rep} beat note, which is much stronger when a larger region of the comb is considered). We send the output to a divide-by-15 frequency divider, and then downmix the signal with a local oscillator operating at 33 MHz to obtain the error signal. The offset beat ξ has more high frequency noise than $f_{rep,}$ as we might expect, because it is affected not only by the pump frequency instability but also by high frequency noise in pump power that is not fully compensated by f_{rep} stabilization, the frequency divider is therefore necessary to reduce the high frequency noise and increase the efficacy of the lock. The error signal is sent to a PI^2D lock box which provides a feedback signal to modulate the diode current of our ECDL which stabilizes the pump frequency. Similar to the feedback to lock f_{rep}, we use a slower secondary feedback (derived from the integrated primary feedback control signal) via the piezo controller of the ECDL to increase dynamic range and preserve the lock for a longer time. We have included a detailed discussion of the feedback locking mechanism in the Methods section of the main text.

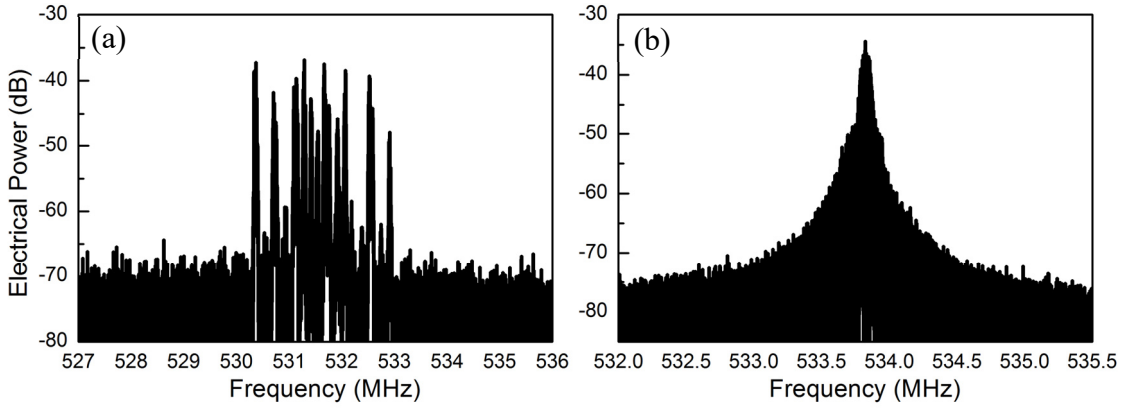

Supplementary Figure S6. a, The measured offset beat ξ at an RBW of 100 kHz when the f_{rep} is not stabilized. The high noise in the beat arises because the offset frequency Δ depends on pump

frequency and intracavity power given by $\Delta = \frac{1}{\sqrt{\pi c|\beta_2|}}\sqrt{\eta\left(n_g f_p - N\frac{n_g^2}{n_0}f_{rep} - \frac{\gamma c P_{int}}{\pi}\right)}$ and since $\xi = \Delta - \left\lfloor\frac{\Delta}{f_{rep}}\right\rfloor f_{rep}$, fluctuations in both pump frequency and f_{rep} add to instability in ξ. **b,** The measured offset beat ξ at an RBW of 10 kHz after f_{rep} is stabilized. We observe an increase in stability of ξ after stabilization of f_{rep} (and thereby stabilization of pump power). Residual noise in the beat note is due to pump frequency noise (and residual noise in pump power after f_{rep} stabilization). ξ can therefore be used to sense pump frequency fluctuations and stabilize it via feedback.

Supplementary Note IV: Derivation of the modulation instability (MI) gain peak

We investigate the intracavity MI gain and derive the frequency at which it is maximum. Supplementary Equation S1, written below describes the cavity boundary conditions and Supplementary Equation S2 describes the wave propagation in the cavity when subject to chromatic dispersion and the Kerr nonlinearity [SR3]:

$$E^{n+1}(0,t) = \sqrt{\rho}E^{n}(L,t)exp(i\varphi_0) + \sqrt{T}E_i, \qquad (S1)$$

$$\frac{\partial E^{n}(z,t)}{\partial z} = -i\frac{\beta_2}{2}\frac{\partial^2 E^{n}(z,t)}{\partial t^2} + i\gamma|E^{n}(z,t)|^2 E^{n}(z,t), \qquad (S2)$$

Under the normalization $U^{n} = \sqrt{\gamma L}E^{n}$; $\kappa = \frac{z}{L}$; $\tau = \frac{t}{\sqrt{|\beta_2|L}}$, the NLSE is reduced to $U_\kappa^n = -i\left(\frac{\eta}{2}\right)U_{\tau\tau}^{n} + i|U^{n}|^2U^{n}$ where $\eta = \frac{\beta_2}{|\beta_2|}$. (To model this [SR5-SR7], here we used the more general NLSE model instead the LLE, the latter which resides under the good cavity limit and the approximation that the evolution is slow compared to round trip time.) Assume steady-state continuous wave in the cavity, one such solution is: $U^{n}(\kappa,\tau) = U_0 exp(i|U_0|^2\kappa)$. A periodic fluctuation generated by instability is modelled by:

$$U^{n}(\kappa,\tau) = [U_0 + v^{n}(\kappa)\times exp(i\Omega\tau) + v^{-n}(\kappa)\times exp(-i\Omega\tau)]exp(i|U_0|^2\kappa)$$

Here Ω corresponds to the location of peak MI as will be derived subsequently. An important point to note here is that Ω may not be an exact multiple of the (normalized) f_{rep}. Substituting this in the NLSE yields after some algebra that:

$$\frac{\partial v^{n}}{\partial\xi}exp(i\Omega\tau) + \frac{\partial v^{-n}}{\partial\xi}exp(-i\Omega\tau)$$
$$= \frac{i\eta\Omega^2}{2}\left(v^{n}exp(i\Omega\tau) + v^{-n}exp(-i\Omega\tau)\right)$$
$$+ i\left(\left(|U_0|^2v^{n} + {U_0}^2v^{-n^*}\right)exp(i\Omega\tau) + \left(|U_0|^2v^{-n} + {U_0}^2v^{n^*}\right)exp(-i\Omega\tau)\right)$$

This then can be written as:

$$\frac{\partial}{\partial\xi}\begin{pmatrix} v^{\mathrm{n}} \\ v^{-\mathrm{n}*} \end{pmatrix} = \begin{bmatrix} \frac{i\eta\Omega^2}{2} + i|U_0|^2 & iU_0{}^2 \\ -i(U_0{}^*)^2 & \frac{-i\eta\Omega^2}{2} - i|U_0|^2 \end{bmatrix}\begin{pmatrix} v^{\mathrm{n}} \\ v^{-\mathrm{n}*} \end{pmatrix}$$

The general solution to the equation above can be written as:

$$\begin{pmatrix} v^{\mathrm{n}} \\ v^{-\mathrm{n}*} \end{pmatrix} = \begin{pmatrix} a^{\mathrm{n}} \\ b^{\mathrm{n}} \end{pmatrix} exp(\mu\kappa) + \begin{pmatrix} c^{\mathrm{n}} \\ d^{\mathrm{n}} \end{pmatrix} exp(-\mu\kappa)$$

With eigenvalue $\mu = \Omega\sqrt{-\eta|U_0|^2 - \Omega^2/4}$ (S3) and eigenvector components satisfying:

$$\frac{a^{\mathrm{n}}}{b^{\mathrm{n}}} = \frac{-(U_0)^2}{\left(\frac{\eta\Omega^2}{2} + |U_0|^2 + i\mu\right)}\ ;\ \frac{d^{\mathrm{n}}}{c^{\mathrm{n}}} = \frac{-(U_0{}^*)^2}{\left(\frac{\eta\Omega^2}{2} + |U_0|^2 + i\mu\right)}$$

Now including the cavity boundary conditions (by substituting E_{n} in Supplementary Eq S1) and noting that E_{i} is a constant, we see that we can write:

$$v^{\pm(\mathrm{n}+1)}(\kappa = 0) = \sqrt{\rho}exp(i\varphi_0 + i|U_0|^2)v^{\pm\mathrm{n}}(\kappa = 1)$$

Since

$$\begin{pmatrix} v^{\mathrm{n}} \\ v^{-\mathrm{n}*} \end{pmatrix} = \begin{bmatrix} 1 & 1 \\ \frac{\left(\frac{\eta\Omega^2}{2} + |U_0|^2 + i\mu\right)}{-(U_0)^2} & \frac{-(U_0{}^*)^2}{\left(\frac{\eta\Omega^2}{2} + |U_0|^2 + i\mu\right)} \end{bmatrix}\begin{pmatrix} a^{\mathrm{n}} \\ c^{\mathrm{n}} \end{pmatrix}$$

And

$$\begin{pmatrix} v^{\mathrm{n}+1} \\ v^{-(\mathrm{n}+1)^*} \end{pmatrix} = \sqrt{\rho}\begin{bmatrix} exp(i\varphi_0 + i|U_0|^2) & 0 \\ 0 & exp(-i\varphi_0 - i|U_0|^2) \end{bmatrix}\begin{pmatrix} v^{\mathrm{n}} \\ v^{-\mathrm{n}*} \end{pmatrix}$$

We can write after substituting in:

$$\begin{pmatrix} a^{\mathrm{n}+1} \\ c^{\mathrm{n}+1} \end{pmatrix}$$

$$= \frac{\sqrt{\rho}}{t^2 - |s|^2}\begin{bmatrix} -|s|^2 & st \\ t^2 & -st \end{bmatrix}\begin{bmatrix} exp(i\varphi_0 + i|U_0|^2) & 0 \\ 0 & exp(-i\varphi_0 - i|U_0|^2) \end{bmatrix}\begin{bmatrix} e^{\mu} & e^{-\mu} \\ te^{\mu}/s & s^*/(at) \end{bmatrix}\begin{pmatrix} a^{\mathrm{n}} \\ c^{\mathrm{n}} \end{pmatrix}$$

, where $s = -(U_0)^2;\ t = \frac{\eta\Omega^2}{2} + |U_0|^2 + i\mu\ ;\ \vartheta = \varphi_0 + |U_0|^2$.

Taking the determinant of this matrix we arrive at the eigenvalues as:

$q_{\pm} = \sqrt{\rho}\left(p \pm \sqrt{p^2 - 1}\right)$ where $p = \frac{-|s|^2(e^{-\mu}e^{-i\vartheta} + e^{\mu}e^{i\vartheta}) + t^2(e^{\mu}e^{-i\vartheta} + e^{-\mu}e^{i\vartheta})}{2(t^2 - |s|^2)}$

Under the mean field approximation, which in this case means that $\mu \sim O(\varepsilon)$, we can approximate e^{μ} to first order as 1+μ, rewriting this equation $p = \cos(\vartheta) - i\mu\sin(\vartheta)\frac{(t^2 + |s|^2)}{(t^2 - |s|^2)}$. Now we see that

$t + |s| = \frac{-\mu^2}{2\eta\Omega^2} + i\mu$ and utilizing (S3), we can rewrite $i\mu\mu\sin(\vartheta)\frac{(t^2+|s|^2)}{(t^2-|s|^2)}$ as $i\mu\sin(\vartheta)\frac{(\frac{-\mu^2}{2\eta\Omega^2}+i\mu)}{(\frac{-\mu^2}{2\eta\Omega^2}+i\mu-2|s|)} - i\mu\sin(\vartheta)\frac{2t|s|}{(\frac{-\mu^2}{2\eta\Omega^2}+i\mu)(\frac{-\mu^2}{2\eta\Omega^2}+i\mu-2|s|)}$ (S4)

Now the first term of (S4) is of order μ^2 and is neglected while the second term reduces to $t = \frac{\eta\Omega^2}{2} + |U_0|^2 + i\mu$ and since μ is small, this is simply $\frac{\eta\Omega^2}{2} + |U_0|^2$. So $p = \cos(\vartheta) - \left(|U_0|^2 + \frac{\eta\Omega^2}{2}\right)\sin(\vartheta)$ (S5). We note that $q_+ = \sqrt{\rho}\left(p + \sqrt{p^2-1}\right)$ is the (largest) eigenvalue of interest and takes its maximum for large p.

Now we write $\vartheta = 2m\pi - \delta + |U_0|^2$ where δ is the detuning from resonance. Applying the good cavity limit we state that both the detuning δ and the additional phase added per round trip due to self-phase modulation $|U_0|^2$, are small in comparison to 2π. Further the good cavity limit ensures that $\rho \to 1$, we introduce the parameter θ = 1-ρ where $\theta \sim O(\varepsilon)$. Subsequently (following [SR5]) we find that to first order the eigenvalue q_+ can be written as

$$q_+ = 1 - \frac{\theta}{2} + \sqrt{4\left(\delta - \frac{\eta\Omega^2}{2}\right)|U_0|^2 - \left(\delta - \frac{\eta\Omega^2}{2}\right)^2 - 3|U_0|^4} \quad (S6)$$

And the maxima of this eigenvalue is obtained at $\Omega_{\text{opt}} = \sqrt{2\,\eta(\delta - 2|U_0|^2)}$ which is the frequency at which MI gain is maximum.

Now δ can be written as $\frac{2\pi(f_\text{p}-f_\text{o})}{f_\text{rep}}$ where f_p is the pump frequency, f_rep is the comb spacing and f_o is the resonance frequency, f_rep can also be expressed as $c/(n_\text{g}L)$ and $f_\text{o} = N\frac{n_\text{g}}{n_\text{o}}f_\text{rep}$ where n_g is the group index and n_o is the refractive index. Furthermore $\omega = \Omega/\sqrt{|\beta_2|L}$ where ω is the frequency with respect to real time coordinates and $|U_0|^2 = \gamma L|E_\text{o}|^2$ where $|E_\text{o}|^2$ is the intracavity power, denoted by P_int.

Putting these together we have:

$$\omega_\text{opt} = \sqrt{\frac{4\pi n_\text{g}\left(f_\text{p} - N\frac{n_\text{g}}{n_0}f_\text{rep}\right)}{\eta|\beta_2|c} - \frac{4\gamma P_\text{int}}{\eta|\beta_2|}} \quad (S7)$$

This formula is intended as an approximation for the case when there is no mode interaction and close to the onset of MI. It illustrates that the breather frequency ξ is dependent only on the two

parameters P_{int} and f_p controlled by pump power and pump frequency respectively. Therefore when the pump power is locked via feedback (utilizing f_{rep} as the indicator of intracavity power), ξ is only dependent on pump frequency f_p. The addition of periodic mode interaction and the effects of "mode pinning" after breather comb formation introduce further complications that can be simulated in the LLE.

To perform the simulations, we first introduce a periodic mode interaction in the LLE via mode shifts (following [SR8]) at resonances every 4 nm. The generated comb spectrum is plotted in Supplementary Fig. S7a, we note the presence of equally spaced subcombs that are on the verge of merging similar to our generated spectrum. Supplementary Fig S7b, plots the comb evolution with detuning swept over 100 MHz, illustrating the large stability region of our comb. We then

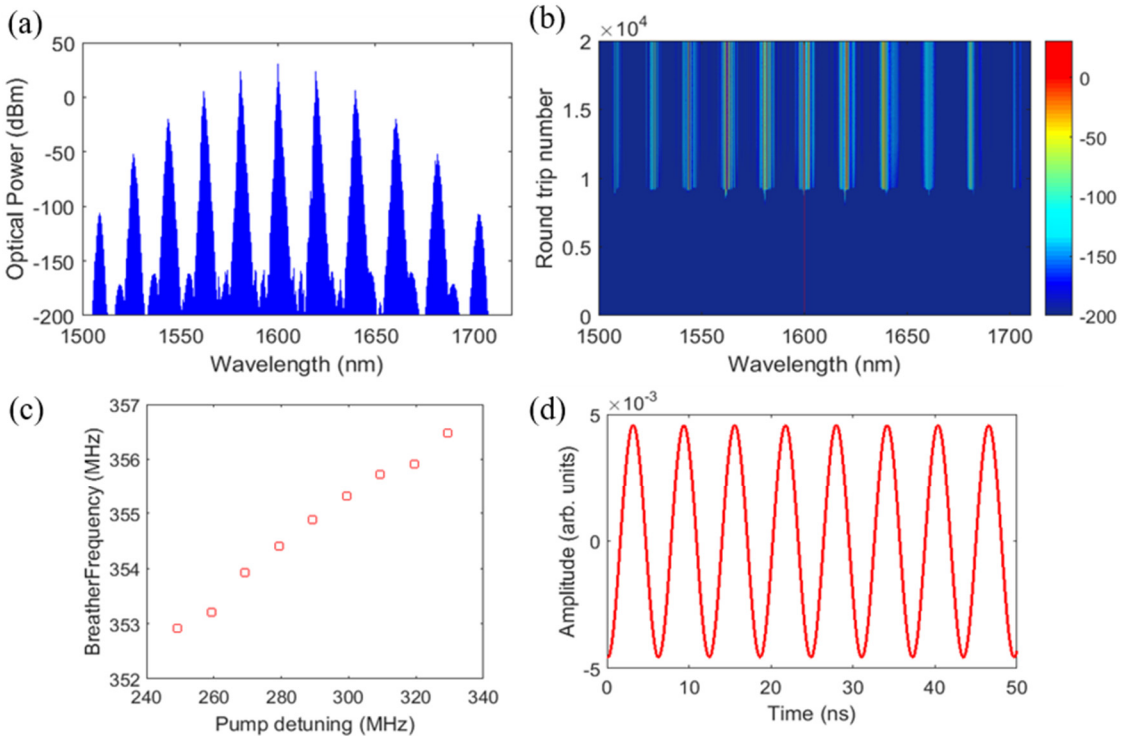

Supplementary Figure S7. a, The simulated breather comb spectrum with multiple equally spaced subcombs. **b,** Evolution of the comb spectrum in the cavity with detuning swept over 200 MHz. The spectrogram shows onset of MI at mode 20, which is disrupted in the simulation due to mode interaction and hence allows the comb to be seeded when dispersion is normal at 30 fs^2/mm. **c**, Shows the breather frequency ξ, when pump detuning is increased and intracavity power is kept constant via a simulated PID loop. We note here that since ξ, depends *both* on the pump detuning and pump power, locking the power provides a direct relationship between breather frequency and pump detuning. **d,** The slow oscillation of the relative phase between the pump and primary comb line, which manifests as the breather is plotted in time.

note that the breathing frequency can in fact be seen as a slow relative phase oscillation between the pump and the first primary comb line as plotted in Supplementary Fig. S7d. A single cycle of this phase oscillation corresponds to a frequency of about 354 MHz, the breather frequency. In parallel to the phase, there is also a slow intensity oscillation of the comb line at the same 354 MHz that corresponds to energy being transferred from the primary lines to the pump and back. Now, finally to simulate the relationship between breather frequency and pump frequency, in conditions similar to our experiment, we simulate a PI loop to control the *intracavity power* P_{int} using only feedback to pump power. We note here (and in the main text) that since the f_{rep} is only dependent on cavity temperature [SR9], which in turn is entirely dependent on P_{int} (neglecting environment temperature changes), locking f_{rep} via feedback to power must necessarily lock P_{int} . This simulated loop therefore exactly corresponds to the experimentally demonstrated f_{rep} stabilization loop via pump power feedback. The PI corner and bandwidth of the simulated feedback loop is however set at 18 MHz (rather than 200 KHz), for ease of simulation to prevent unreasonably large number of round trips required for the loop to stabilize P_{int}. We subsequently ran the simulation for 5 million roundtrips with PI loop to stabilize P_{int} engaged *and* swept laser detuning while monitor change in breather frequency. Our results are plotted in Supplementary Fig. S7c, the simulated slope of change in breather frequency to change in pump detuning is ~ 45 KHz/MHz.

Supplementary Note V: Out-of-loop characterization

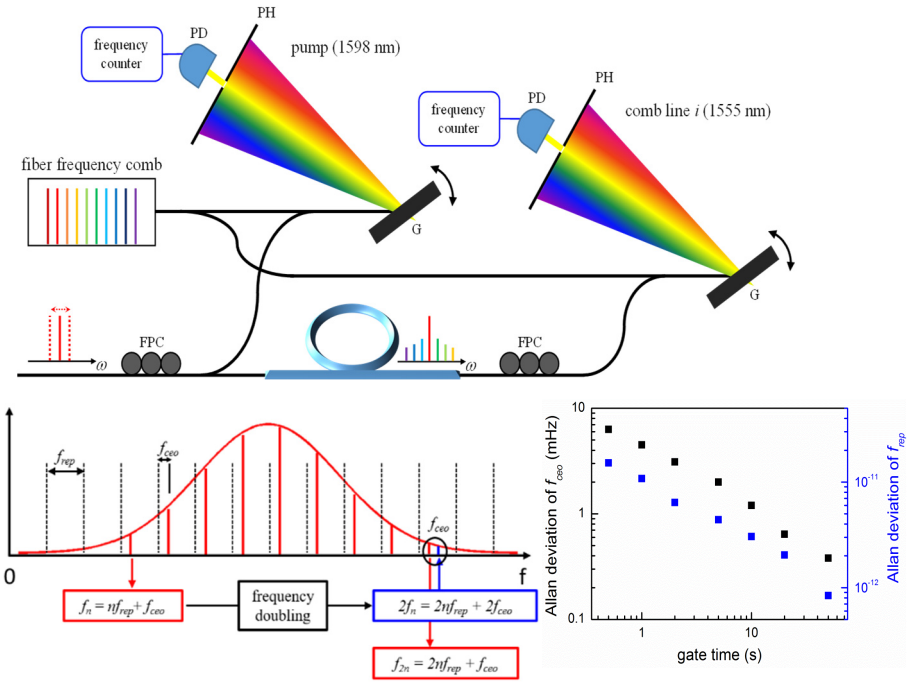

Supplementary Figure S8. a, To quantify the frequency instability of the Kerr frequency comb, two comb lines (pump at 1598 nm and i^{th} comb at 1555 nm) are compared to an independently stabilized FFC and the heterodyne beat frequencies are counted with a 10-digit, Λ-type frequency counter. The FFC is referenced to a rubidium-disciplined crystal oscillator with a frequency fractional instability of 5×10^{-12} at 1 second. The gratings critically remove the unwanted reference FFC comb lines for reliable counting measurements. **b,** The repetition rate of the FFC (≈ 250 MHz) is detected with a PD and locked to an RF local oscillator, in addition, *f-2f* interferometry [SR10-SR12] is used to detect f_{ceo} and lock it to an RF reference with the same clock as that used to lock f_{rep}. **c,** The Allan Deviation of the f_{ceo} is plotted for the FFC in mHz and the Allan Deviation for f_{rep} is plotted relative to the carrier. As we observe from the plot, f_{rep} is the limiting factor for the stability of our reference, which is per our expectation, because of the high sensitivity of the comb line frequencies to f_{rep} due to the low optical division ratio (≈ 10^{-6}).

Supplementary Note VI: Verification of ξ across different chips and breather states

Formation of Kerr combs with a single offset beat in addition to f_{rep} is not a unique property dependent on microresonator characteristics but in fact is general and arises from the mechanics of Kerr comb generation. These combs have also been observed previously in microresonators [SR1, SR13], but with very different characteristics. In addition, to the 18 GHz comb described in the main text, we also observe a similar state in a single mode Si_3N_4 microresonator cavity with a tapered structure [SR14] thereby verifying the applicability of our approach across different breather comb states and chipsets. The comb spectrum is shown in Supplementary Fig. S9a. and

the offset beat is measured in different comb slices, as shown in Supplementary Fig. S9b, to verify that it is truly a single offset comb state. Breather combs in general have a modulated spectrum such as in Supplementary Fig. S9a, this may limit performance in some applications such as the spectral density in dense-wavelength optical communications. However, breather solitons can provide both the breathing frequency for locking while having a smooth spectrum for various applications for further studies.

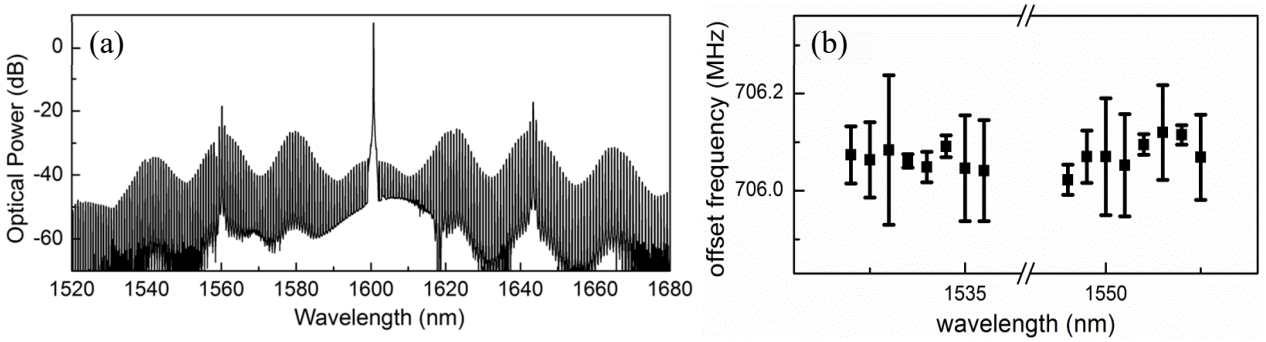

Supplementary Figure S9. a, Spectrum of a comb-state, similar to the one we stabilize, generated in a single mode microresonator with a tapered structure. This comb state generates a single offset beat ξ in the RF domain in addition to the repetition rate. **b,** To verify that the offset frequency is uniquely defined across the whole Kerr frequency comb, we measure it at various different spectral segments with a tunable filter (0.22 nm FWHM filter bandwidth). Free-running ξ without f_{rep} stabilization (≈ 700 MHz) in different spectral regions is measured to be the same within error bars of ≈ 200 kHz. At wavelengths where the beat notes have SNR higher than 10 dB (100 kHz RBW), 10 measurements are taken to determine the mean value of the offset frequency. The error bar of the measurement is defined as the peak-to-peak deviation from the 10 measurements.

Supplementary Note VII: Verification of stabilization of f_{rep} stabilization after locking ξ

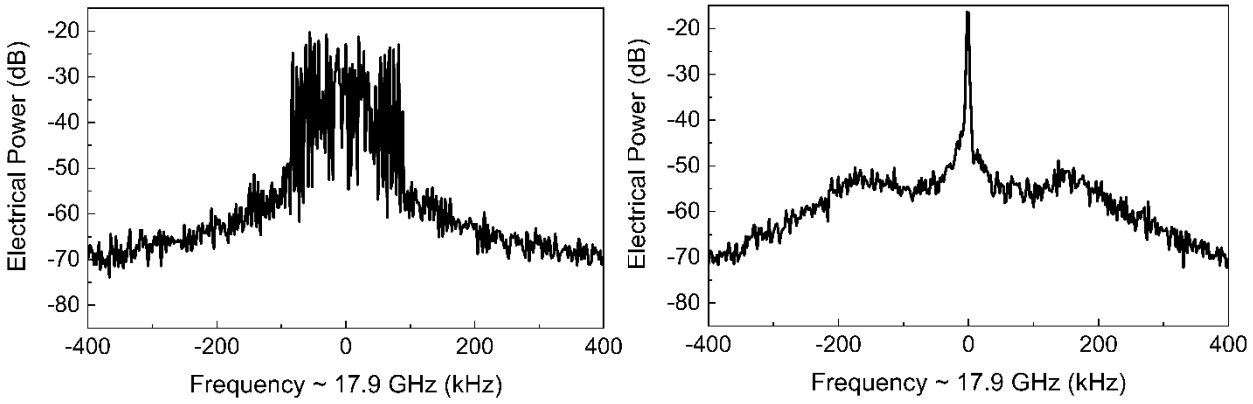

Supplementary Figure S10. a, f_{rep} measured at an RBW of 1 kHz before locking ξ but after locking pump frequency, **b,** f_{rep} measured after locking ξ at an RBW of 1 kHz. Locking sidebands are observed at ≈ 200 kHz, corresponding to the PI corner of the feedback loop intended to stabilize ξ. Stabilization of f_{rep} is clearly observed subsequent to locking ξ. Furthermore, as explained in the

main text, we expect the phase noise of this signal to be ≈ 38 dB lower than the phase noise of the locked signal ξ after division to the same carrier.

Supplementary References:

[SR1] T. Herr, K. Hartinger, J. Riemensberger, C. Y. Wang, E. Gavartin, R. Holzwarth, M. L. Gorodetsky, and T. J. Kippenberg, Universal formation dynamics and noise of Kerr-frequency combs in microresonators, *Nat. Photon.* **6**, 480 (2012).

[SR2**]** M. Yu, J. K. Jang, Y. Okawachi, A. G. Griffith, K. Luke, S. A. Miller, X. Ji, M. Lipson, and A. L. Gaeta, Breather soliton dynamics in microresonators, *Nat. Commun.* **8**, 14569 (2017).

[SR3] A. S. Raja, A. S. Voloshin, H. Guo, S. E. Agafonova, J. Liu, A. S. Gorodnitskiy, M. Karpov, N. G. Pavlov, E. Lucas, R. R. Galiev, A. E. Shitikov, J. D. Jost, M. L. Gorodetsky, and T. J. Kippenberg, Electrically pumped photonic integrated soliton microcomb, *Nat Commun* **10,** 680 (2019).

[SR4] A. S. Raja, J. Liu, N. Volet, R. N. Wang, J. He, E. Lucas, R. Bouchandand, P. Morton, J. Bowers, and T. J. Kippenberg, Chip-based soliton microcomb module using a hybrid semiconductor laser, *Opt. Express* **28**, 2714 (2020).

[SR5] S. Coen and M. Haelterman, Modulational instability induced by cavity boundary conditions in a normally dispersive optical fiber, *Phys. Rev. Lett.* **79**, 4139 (1997).

[SR6] A. Pasquazi, M. Peccianti, L. Razzari, D. J. Moss, S. Coen, M. Erkintalo, Y. K. Chembo, T. Hansson, S. Wabnitz, P. Del'Haye, X. Xue, A. M. Weiner, and R. Morandotti, Micro-combs: a novel generation of optical sources, *Phys. Rep.* **729**, 1 (2018).

[SR7] Y. K. Chembo, D. Gomila, M. Tlidi, and C. R. Menyuk, Theory and applications of the Lugiato-Lefever equation, *Eur. Phys. J. D* **71**, (2017).

[SR8] D.C. Cole, E.S. Lamb, P. Del'Haye, S.A. Diddams, and S. B. Papp, Soliton crystals in Kerr resonators, *Nature Photon* **11**, 671 (2017).

[SR9] J. R. Stone, T. C. Briles, T. E. Drake, D. T. Spencer, D. R. Carlson, S. A. Diddams, and S. B. Papp, Thermal and nonlinear dissipative-soliton dynamics in Kerr-microresonator frequency combs, *Phys. Rev. Lett.* **121**, 063902 (2018).

[SR10] D. J. Jones, S. A. Diddams, J. K. Ranka, A. Stentz, R. S. Windeler, J. L. Hall, and S. T. Cundiff, Carrier-envelope phase control of femtosecond mode-locked lasers and direct optical frequency synthesis, *Science* **288**, 635 (2000).

[SR11] V. Brasch, E. Lucas, J. D. Jost, M. Geiselmann, and T. J. Kippenberg, Self-referenced photonic chip soliton Kerr frequency comb, *Light: Sci. & Appl.* **6**, 16202 (2017).
[SR12] T. C. Briles, J. R. Stone, T. E. Drake, D. T. Spencer, C. Fredrick, Q. Li, D. Westly, B. R. Ilic, K. Srinivasan, S. A. Diddams, and S. B. Papp, Interlocking Kerr-microresonator frequency combs for microwave to optical synthesis, *Opt. Lett.* **43**, 2933 (2018).
[SR13] S. B. Papp, P. Del'Haye, and S. A. Diddams, Parametric seeding of a microresonator optical frequency comb, *Opt. Express* **21**, 17615 (2013).
[SR14] S.-W. Huang, H. Liu, J. Yang, M. Yu, D.-L. Kwong, C. W. Wong, Smooth and flat phase-locked Kerr frequency comb generation by higher order mode suppression, *Sci. Rep.* **6**, 26255 (2016).